Influence of electrolyte temperature on the synthesis of iron oxide nanostructures by electrochemical anodization for water splitting.

Bianca Lucas-Granados, Rita Sánchez-Tovar, Ramón M. Fernández-Domene, José García-Antón*

Ingeniería Electroquímica y Corrosión (IEC). Instituto Universitario de Seguridad Industrial, Radiofísica y Medioambiental (ISIRYM). Universitat Politècnica de València. Camino de Vera s/n, 46022 Valencia, Spain.

* jgarciaa@iqn.upv.es

Abstract

Iron oxide nanostructures are an attractive option for being used as photocatalyst in photoelectrochemical applications such as water splitting for hydrogen production. Nanostructures can be obtained by different techniques, and electrochemical anodization is one of the simplest methods which allows high control of the obtained morphology by controlling its different operational parameters. In the present study, the influence of the electrolyte temperature during electrochemical anodization under stagnant and hydrodynamic conditions was evaluated. Temperature considerably affected the morphology of the obtained nanostructures and their photoelectrochemical behavior. Several techniques were used in order to characterize the obtained nanostructures, such as Field Emission Scanning Electron Microscopy (before and after the annealing treatment in order to evaluate the changes in morphology), Raman spectroscopy, photocurrent vs. potential measurements and Mott-Schottky analysis.

1

Results revealed that the nanostructures synthesized at an electrolyte temperature of 25 ºC and 1000 rpm are the most suitable for being used as photocatalysts for water splitting.

Keywords: iron oxide, nanostructure, electrochemical anodization, electrolyte temperature, water splitting.

1. Introduction

Nowadays, there is an increasing demand of energy production. Renewable energy sources, such as sunlight, are becoming popular since they can produce clean energy contributing to mitigate the global warming [1–7]. Since Fujishima and Honda in 1972 demonstrated that hydrogen generation was possible by photoelectrochemical water splitting using TiO_2 as a photoanode [8], many efforts have been focused on the photoelectrochemical water splitting process [1,9–13]. Different photoanodes materials have been investigated in recent times for water splitting tests, such as TiO_2 [14], WO_3 [15], ZnO [16] and so on, but one of the best options is iron oxide. In particular, hematite (α-Fe_2O_3) possesses a suitable band gap (~ 2.1 eV), which can absorb ~ 40 % of sunlight in the visible region [12,17]. Furthermore, hematite is an n-type semiconductor with different characteristics, such as good chemical stability, abundance in the Earth's crust, low cost, non-toxicity and environmental compatibility, which make it suitable for photoelectrocatalysis applications [18–22]. Nevertheless, some drawbacks, i.e. small hole diffusion length (2-4 nm) and poor minority charge carrier mobility, limit its applications [23–26]. By nanostructuring hematite anodes these challenges can be overcome, making hematite an attractive option for photoelectrochemical applications such as water splitting [21,23,27,28].

Hematite nanostructures can be formed by different methods, i.e. electrochemical anodization [29,30], sol-gel [31,32], hydrothermal method [33,34], electrospinning [35,36], etc. Among them, electrochemical anodization is one of the best techniques because different morphologies for the nanostructures can be obtained by controlling the anodization parameters. Additionally, it is a simple, high controllable, low-cost and attractive method for large-scale production [22,30,37,38]. In previous works, anode rotation speed during the electrochemical anodization process (hydrodynamic conditions were varied from 0 to 3000 rpm) was studied. The conclusion was that hydrodynamic conditions, especially 1000 rpm, enhanced the photoelectrochemical performance of the iron oxide nanostructures [39]. In the present study, electrolyte temperature (from 25 to 60 ºC) during electrochemical anodization of iron has been evaluated in order to characterize the formed nanostructures and to analyze their photoelectrocatalytic performance in applications such as water splitting. Moreover, since rotating the anode (iron rod) at 1000 rpm enhanced the iron oxide nanostructures performance, all the work has been carried out under stagnant and hydrodynamic (1000 rpm) conditions, in order to compare the influence of electrolyte temperature under both conditions.

The morphology of the samples has been characterized by means of Field Emission Scanning Electron Microscopy (FE-SEM), the crystalline structure has been examined using Laser Confocal Raman Microscopy, and the different electrochemical and photoelectrochemical properties of the samples have been analyzed by different techniques, such as photocurrent vs. potential measurements (water splitting), photostability tests, and Mott-Schottky (MS) analysis.

2. Experimental

2.1. Synthesis of the nanostructures

Nanostructures were synthesized by electrochemical anodization of iron rods (purity of 99.9 %). First of all, the surface of the iron rods was abraded with silicon carbide papers (SiC) from 220 to 4000, sonicated in ethanol for 2 minutes, rinsed with distilled water and dried in a nitrogen stream. Then, electrochemical anodization of the iron rods was carried out in an ethylene glycol solution containing 0.1 M of ammonium fluoride and 3 % vol. of water. Anodization was performed at 50 V for 15 minutes, and current density vs. time was continuously measured during the process. For each anodization test, the iron rod (9.5 mm in diameter, i.e. an exposed area to the electrolyte during the electrochemical anodization of 0.7 cm²) was used as working electrode and a platinum foil as counter electrode. Different electrolyte temperatures were tested during the electrochemical anodization: 25, 40, 50 and 60 $^{\circ}$C. Electrolyte temperature was maintained constant during anodization by means of a thermostated bath. Furthermore, the nanostructures were formed under both stagnant and hydrodynamic conditions (connecting the anode to a rotating disk electrode (RDE) coupled to a motor controller), in particular at 0 and 1000 rpm, corresponding to Reynolds number of 0 and 165, respectively, since in a previous work the best photoelectrochemical response was achieved for the nanostructures synthesized at 1000 rpm [39].

After anodization, the nanostructures were rinsed with distilled water, dried in a nitrogen stream and annealed in a tube furnace at 500 $^{\circ}$C for 1 hour in an argon atmosphere. The heating rate was 15 $^{\circ}$C · min^{-1} and the samples were subsequently cooled within the furnace by natural convection [40].

2.2. Morphological characterization of the nanostructures

The characterization of the morphology of the nanostructures (before and after the annealing treatment) was carried out using Field Emission Scanning Electron Microscopy with an extra high tension (EHT) of 3 kV. The images were acquired at 10,000x and 30,000x magnifications.

2.3. Characterization of the crystalline structure

The crystallinity of iron oxide nanostructures was analyzed by means of a Laser Confocal Raman microscope. The characterization was performed using a neon laser 632 nm with ~700 μW.

2.4. Electrochemical and photoelectrochemical characterization

All the electrochemical and photoelectrochemical experiments were performed in a three-electrode configuration. The iron oxide nanostructure was the working electrode, a platinum tip was the counter electrode and an Ag/AgCl (3M KCl) electrode was the reference electrode. The area of the iron oxide nanostructure that was exposed to the solution during the tests was 0.26 cm². The photoelectrochemical experiments were performed using a solar simulator (AM 1.5 conditions at $100 \ mW \cdot cm^{-2}$).

2.4.1. Photoelectrochemical water splitting tests

Photocurrent density vs. potential plots were performed in 1 M KOH by scanning the potential from -0.4 to +0.6 V at a scan rate of $2 \ mV \cdot s^{-1}$, switching the light on and off every 0.02 V (i.e. 0.02 V in the dark and 0.02 V in the light).

5

2.4.2. Photostability measurements

Photostability measurements were carried out leaving the nanostructures in 1 M KOH solution under simulated AM 1.5 illumination for an hour at an applied potential of 0.35 V (vs. Ag/AgCl). The photocurrent density vs. time was continuously measured in order to check the stability against photocorrosion of the nanostructures.

2.4.3. Mott-Schottky analysis

Mott-Schottky analysis were performed both under dark and light conditions in 1 M KOH solution at a constant frequency value of 5 kHz. The potential was started at the Open Circuit Potential (OCP) value of the sample (roughly 0.3 V) and it was swept in the negative direction with an amplitude signal of 0.01 V at a rate of $28 \ mV \cdot s^{-1}$.

3. Results and discussion

3.1. Synthesis of the nanostructures

Figure 1 shows the current density vs. time registers (anodization curves) during the formation of the nanostructures by electrochemical anodization under stagnant (Figure 1 a)) and hydrodynamic conditions (Figure 1 b)).
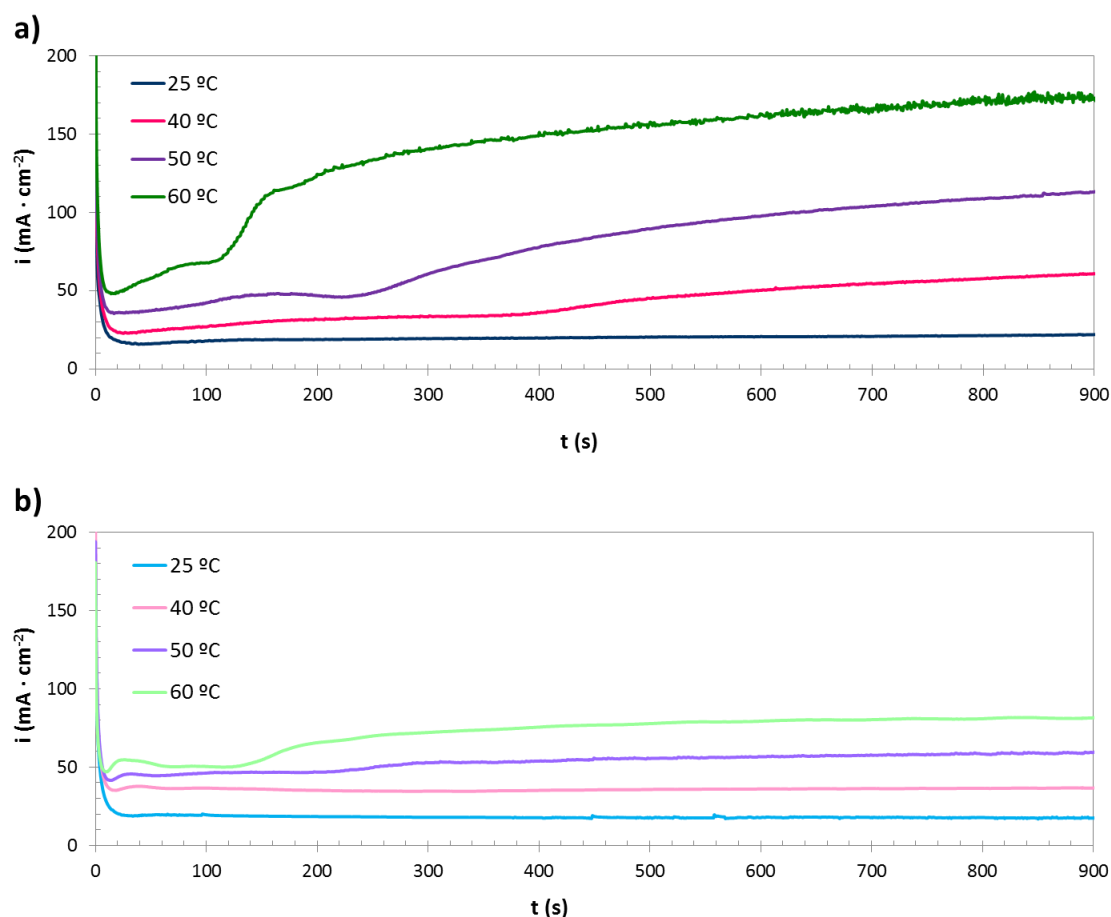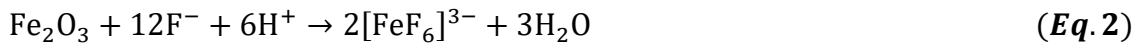
Figure 1. Current density vs. time measurements during electrochemical anodization of iron at the different electrolyte temperatures (25, 40, 50 and 60 $^{\circ}$C). Electrochemical anodization conditions: 50 V for 15 min in an EG solution containing 0.1 M NH$_4$F and 3 %vol. H$_2$O, under stagnant (a) and hydrodynamic (b) conditions.

Note that all the anodization curves exhibit almost the same behavior and the three main characteristic stages of the formation of nanotubular structures can be identified: I) a sharp drop in the current density associated with the formation of an insulating compact oxide layer on the substrate, II) a slightly increase in the current density with time due to the formation of tiny pits in the compact layer because of the action of F$^-$, leading to a nanoporous structure that offers less resistance to the current, and III) a steady state

region owing to the equilibrium between the formation of the oxide layer and its chemical dissolution which conducts to the formation of a nanotubular structure. The reactions that take place during this formation are presented in Eq. 1 (formation of the compact iron oxide layer) and Eq. 2 (partial dissolution of the compact layer due to the F$^-$ ions leading to tiny pits) [29,41–43].

$$2\mathrm{Fe} + 3\mathrm{H_2O} \rightarrow \mathrm{Fe_2O_3} + 6\mathrm{H^+} + 6e^- \qquad\qquad (\boldsymbol{Eq.\,1})$$

$$\mathrm{Fe_2O_3} + 12\mathrm{F^-} + 6\mathrm{H^+} \rightarrow 2[\mathrm{FeF_6}]^{3-} + 3\mathrm{H_2O} \qquad\qquad (\boldsymbol{Eq.\,2})$$

Additionally, Figure 1 a) shows the anodization curves for the samples synthesized by electrochemical anodization under stagnant conditions and at different electrolyte temperatures. The three characteristic regions are identified and the current density increases also with increasing temperature. However, the steady state region is only constant at 25 ^{o}C but it breaks for upper temperatures, leading to a continuous increase in current density with time. This increase in current density appears at lower times and is more pronounced with increasing temperatures, i.e. for 40 ^{o}C the rise in current density starts approximately after the first 420 seconds, for 50 ^{o}C starts at ~ 240 seconds and for 60 ^{o}C at ~ 100 seconds. In fact, the temperature of the electrode (iron rod) increases during electrochemical anodization because of the chemical reactions involved in the process; this phenomenon also occurs in other materials such as aluminum [44,45]. For this reason, when the electrolyte temperature is 40 ^{o}C or higher, the electrode temperature increases and the steady state is broken, resulting in a progressive increase in current density. However, when the electrolyte temperature is 25 ^{o}C, the electrode temperature is maintained almost constant and the current density is also approximately constant as Figure 1 a) shows.

On the other hand, Figure 1 b) shows the anodization curves for the samples synthesized under hydrodynamic conditions. All the curves exhibited the same described behavior, with the three characteristic regions of the formation of nanotubular structures. Under hydrodynamic conditions, the steady state only breaks for 50 ^{o}C and 60 ^{o}C after, approximately, 240 and 140 seconds, respectively. This indicates two important aspects, the first one is that at an electrolyte temperature of 40 ^{o}C and under hydrodynamic conditions the steady state is not broken (in contrast with the curve at 40 ^{o}C under stagnant conditions in Figure 1 a)), because rotating the electrode during anodization homogenizes its temperature and the heat can be easily dissipated to the electrolyte. The second aspect is that the break of the steady state at 50 and 60 ^{o}C under hydrodynamic conditions is smoother than under stagnant conditions, and moreover, the time at which the steady state is broken at 60 ^{o}C under hydrodynamic conditions (~ 140 seconds) increases in comparison to stagnant ones (~ 100 seconds), i.e. the steady state is maintained constant for more time, because of the better dissipation of the heat of the electrode under hydrodynamic conditions.

Moreover, comparing a given electrolyte temperature during anodization for both stagnant and hydrodynamic conditions, the current density in the nanotubes formation region is higher for the samples anodized at 1000 rpm. In fact, the steady state current density is controlled by diffusion processes and rotating the electrode during anodization enhances this process, therefore, higher current densities are obtained [46,47]. However, at 40 ^{o}C (under stagnant conditions) and 50 ^{o}C and 60 ^{o}C (under both conditions), when the steady state is broken and current density significantly increases, the process is not following the typical nanotubular structure formation.

3.2. Morphological characterization of the nanostructures

Field Emission Scanning Electron Microscopy was used for the morphological characterization of the samples synthesized at the different electrolyte temperatures during electrochemical anodization under both stagnant and hydrodynamic conditions. The morphology characterization was performed for the nanostructures before (as-anodized) and after (annealed) the thermal treatment.

On the one hand, Figure 2 shows FE-SEM images of the samples anodized at the different temperatures under stagnant conditions (0 rpm) and before the annealing treatment. Figures 2 a)-b) show that at an electrolyte temperature of 25 °C the morphology of the iron oxide nanostructures was nanotubular with some initiation layer that partially covered the entrances of the tubes. However, when electrolyte temperature increased until 40 °C (Figures 2 c)-d)) the nanotubular structure was collapsed and only a few nanotubes/nanopores were visible in some regions. At 50 °C, Figures 2 e)-f) show that the nanostructure was collapsed with no nanotubular/nanoporous regions visible but with small granular-like regions, and finally, when electrolyte temperature rose up to 60 °C (Figures 2 g)-h)) the nanostructure completely disappeared and the morphology corresponded to a granular-like layer which is in agreement with the break of the steady state current density associated with the formation of nanotubular structures showed in Figure 1 a). This change in the morphology from 25 °C to higher temperatures is due to the increase in the electrolyte temperature that leads to an increase in the electrode temperature, making the morphology collapse and become more compact. This is in agreement with the current density vs. time plots (Figure 1 a)) that indicated that at 25 °C the steady-state current density was maintained (i.e. the equilibrium between the formation of the oxide layer and its chemical dissolution leading to the formation of a

nanotubular structure was reached). Then, the behavior of this curve corresponded to a typical nanotubular structure formation. However, as Figure 1 a)) shows, at electrolyte temperatures of 40 °C or higher, this equilibrium was disrupted and the current density rapidly increased.
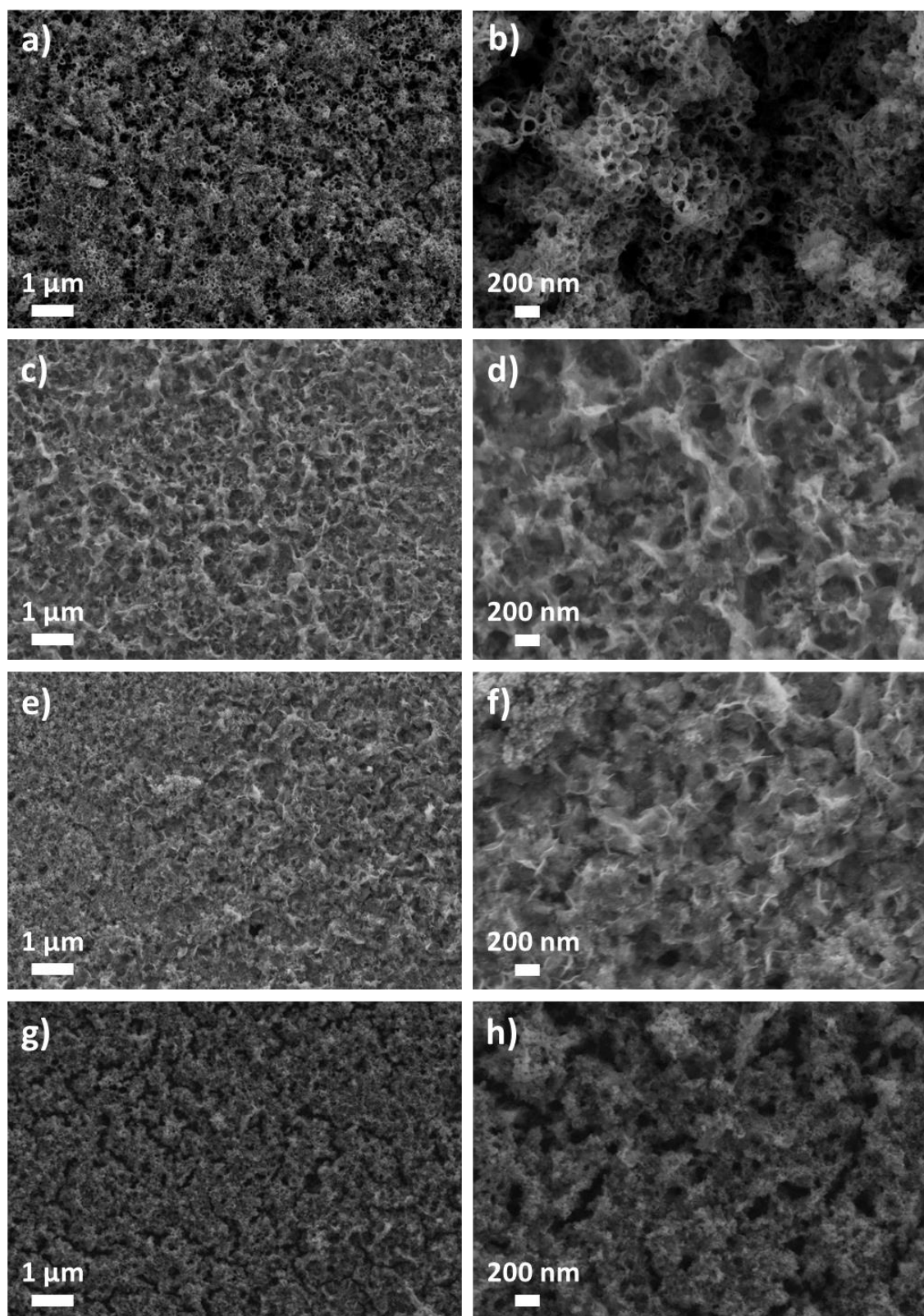
Figure 2. FE-SEM images of the as-anodized nanostructures synthesized at the different electrolyte temperatures: a-b) 25 °C, c-d) 40 °C, e-f) 50 °C and g-h) 60 °C, under stagnant conditions.

On the other hand, FE-SEM images of the nanostructures synthesized under hydrodynamic conditions (1000 rpm) and before the annealing treatment are presented in Figure 3. As it can be observed in Figures 3 a)-b), the nanostructures synthesized at 25 ^{o}C and 1000 rpm were also nanotubular as it occurred at 25 ^{o}C and 0 rpm. However, comparing the nanostructure synthesized at 1000 rpm, it did not present the initiation layer and it was more homogeneous than in the case of stagnant conditions. This indicates that working under hydrodynamic conditions and at 25 ^{o}C enhanced the formation of a homogeneous nanotubular structure. Moreover, Figures 3 c)-d) show that at 40 ^{o}C and 1000 rpm the formed nanostructure was also nanotubular. This nanostructure synthetized at 40 ^{o}C and 1000 rpm was completely different compared to the nanostructure anodized at 40 ^{o}C and 0 rpm, since in the latter case the nanotubular structure almost disappeared. According to these results, working under hydrodynamic conditions at 40 ^{o}C are an important and determining factor in the formation of iron oxide nanostructures, since at 0 rpm the nanostructure was collapsed and stacked whereas at 1000 rpm the structure was nanotubular. This is in agreement with the anodization curves (Figure 1 b)) which indicated that anodizing at 40 ^{o}C and 1000 rpm a steady state was observed, indicating the typical curve of the formation of a nanotubular structure.
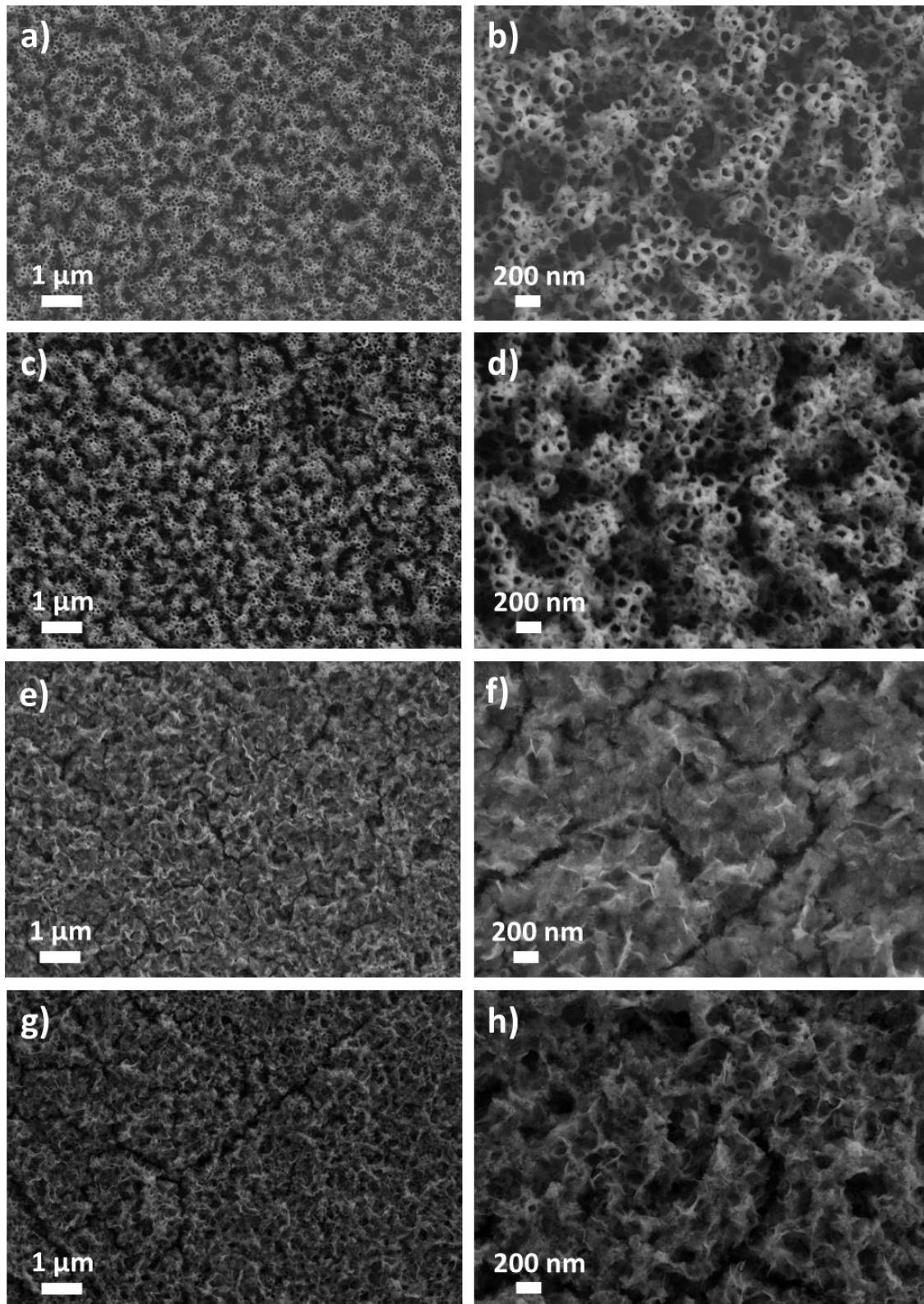
Figure 3. FE-SEM images of the as-anodized nanostructures synthesized at the different electrolyte temperatures: a-b) 25 ⁰C, c-d) 40 ⁰C, e-f) 50 ⁰C and g-h) 60 ⁰C, under hydrodynamic conditions.

By contrast, Figures 3 e)-f) show a collapsed nanostructure for the sample anodized at 50 $^{\circ}$C and 1000 rpm, very similar to the one synthesize at 0 rpm at this temperature, but without the presence of a granular-like region. Finally, at 60 $^{\circ}$C and 1000 rpm Figures 3 g)-h) show a collapsed nanostructure with no significant differences in morphology compared to the one synthesized at 50 $^{\circ}$C (Figures 3 e)-f)). According to the anodization curves presented in Figure 1 b), at 50 $^{\circ}$C and 60 $^{\circ}$C (under hydrodynamic conditions) the steady state was broken, indicating that the behavior was not the typical for the nanotubular structure formation. In conclusion, electrolyte temperatures of 25 $^{\circ}$C (under stagnant and hydrodynamic conditions) and 40 $^{\circ}$C (under hydrodynamic conditions) promoted the formation of nanotubular structures of iron oxide. However, when the electrolyte temperature was higher than 25 $^{\circ}$C under stagnant conditions or higher than 40 $^{\circ}$C under hydrodynamic conditions, the nanostructures became more compact and collapsed. Regarding temperatures of 50 and 60 $^{\circ}$C, there were not significant differences in morphology for the nanostructures obtained under stagnant or hydrodynamic conditions. This notable change in the morphology at high electrolyte temperatures, showing no nanotubular structure, could be because of the fact that temperature favored the dissolution of the compact layer due to the F^{-} ions (Eq. 2), hence, the nanotubes were dissolved and they disappeared from the surface. Moreover, the use of higher temperatures during anodization can improve the diffusion rate of Fe ions with higher thermal kinetic energy, then, the Fe_2O_3 etching rate was also faster [5].

Analyzing FE-SEM images for the samples anodized at different electrolyte temperatures under stagnant conditions and annealed for 1 hour at 500 $^{\circ}$C in an argon atmosphere at a heating rate of 15 $^{\circ}$C $\cdot$ min^{-1}, there are significant differences with respect to the as-anodized ones. Firstly, Figures 4 a)-b) show that at 25 $^{\circ}$C the

nanostructures became more compact in comparison to the as-anodized ones with the pores conglomerating and some nanosheets appearing over the entire surface. At 40 °C, as Figures 4 c)-d) illustrate, only a few nanosheets appeared over the surface but the pores were more conglomerated leading to a more compact structure, very similar to the sample anodized at 50 °C (Figures 4 e)-f)) that was more compact but the nanosheets did not practically appear. Finally, for the sample anodized at 60 °C (Figures 4 g)-h)) the structure was different since it was formed by shorter nanosheets aggregated in clusters and some crystals precipitated over the surface. The morphology of the nanostructures presented in Figure 4 indicates that annealing process favored the compactness of the nanostructures and the appearance of some nanosheets or single-crystals depending on the electrolyte temperature during electrochemical anodization.
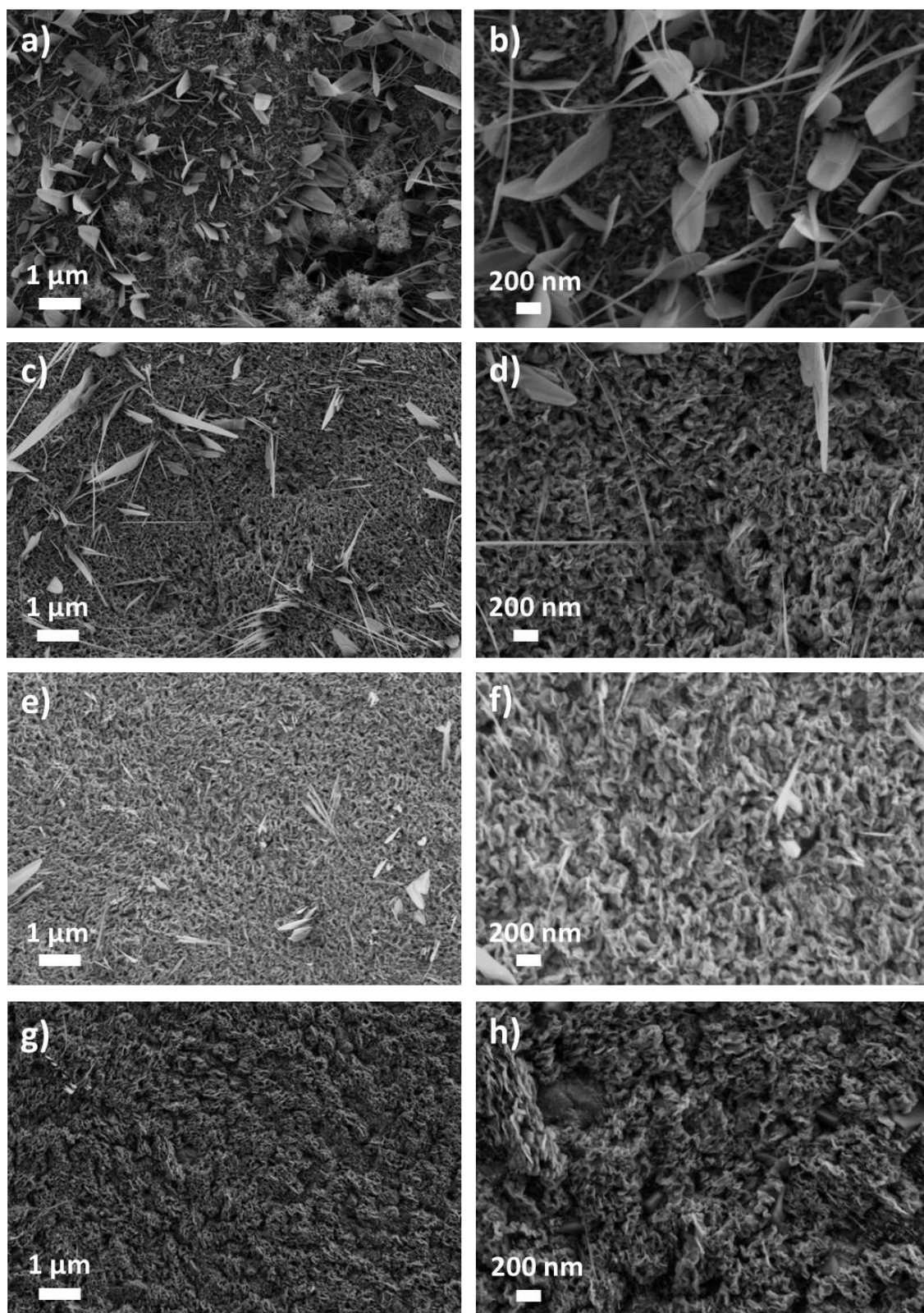
Figure 4. FE-SEM images of the nanostructures synthesized at the different electrolyte temperatures: a-b) 25 ⁰C, c-d) 40 ⁰C, e-f) 50 ⁰C and g-h) 60 ⁰C under stagnant conditions and annealed at 500 ⁰C in argon for 1 h.

Concerning the samples anodized under hydrodynamic conditions and annealed for 1 hour at 500 ℃ in an argon atmosphere at a heating rate of 15 ℃ · min^{-1}, the nanostructures were similar to the ones synthesized at 0 rpm and annealed at the same conditions. Figures 5 a)-b) indicate that at 25 ℃ the nanostructures were more compact with the pores conglomerating and some nanosheets appearing over all the surface but in less quantity than in the case of the nanostructures synthesized under stagnant conditions and annealed (Figures 4 a)-b)). At 40 ℃, Figures 5 c)-d) show that the pores were more conglomerated and the nanosheets were less abundant over the surface. In the case of 50 ℃ (Figures 5 e)-f)) the structure was more compact and the nanosheets were hardly present. Lastly, at 60 ℃ (Figure 5 g)-h)) the morphology of the nanostructure was composed by shorter nanosheets aggregated in clusters and some single-crystals (more than in the case of the samples anodized at 0 rpm and annealed at the same conditions, as Figures 4 g)-h) showed).
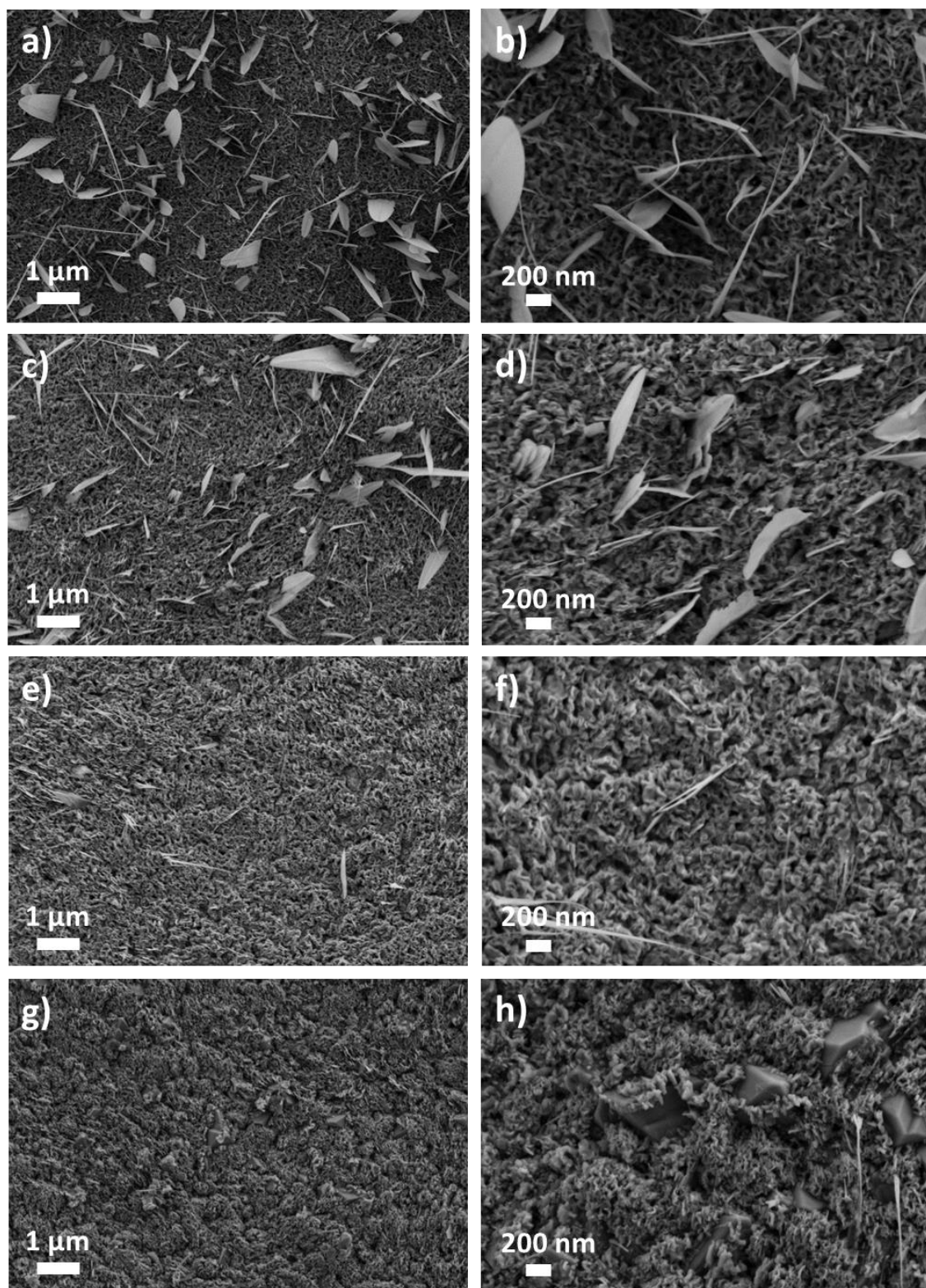
Figure 5. FE-SEM images of the nanostructures anodized at the different electrolyte temperatures: a-b) 25 ⁰C, c-d) 40 ⁰C, e-f) 50 ⁰C and g-h) 60 ⁰C under hydrodynamic conditions, and annealed at 500 ⁰C in argon for 1 h.

3.3. Characterization of the crystalline structure

Figure 6 presents the Raman spectra of all the samples anodized at the different electrolyte temperatures and annealed in an argon atmosphere at 500 º C for 1 hour at a heating rate of 15 º C · min^{-1}. The structure of the as-anodized samples is amorphous in nature, and it is well known that a crystalline structure is necessary in order to use the material as photocatalyst, hence, an annealing treatment is needed. Once the structure of the samples is crystalline, they can be used as photocatalyst in different photoelectrochemical applicacions such as water splitting. Annealing conditions were studied in a previous work in order to find the best conditions for the formation of iron oxide nanostructures for photocatalysis [40]. As Figure 6 shows, the peaks for all the samples appeared at the same Raman shifts. Most of the peaks in the spectra were associated with the hematite structure, and they appeared at: 229 cm^{-1} (A_{1g}), 249 cm^{-1} (E_g), 295 cm^{-1} (E_g), 414 cm^{-1} (E_g), 500 cm^{-1} (A_{1g}), 615 cm^{-1} (E_g) and 1317 cm^{-1} (2nd order). However, some peaks appeared at Raman shifts that indicate a magnetite structure, i.e. 554 cm^{-1}, 672 cm^{-1} and ~ 820 cm^{-1} [48–51]. Then, all the nanostructures were composed mainly of α-Fe_2O_3 with some amount of Fe_3O_4. However, some of the peaks associated with hematite phase seemed to start to disappear at higher electrolyte temperatures regardless the anodization conditions, which indicated a predominant hematite phase but with a little less proportion of hematite in comparison to the samples anodized at lower electrolyte temperatures. Thus, an increase in electrolyte temperature during anodization promoted the formation of nanostructures with apparently less hematite in spite of having a predominant hematite phase in their crystalline structure.
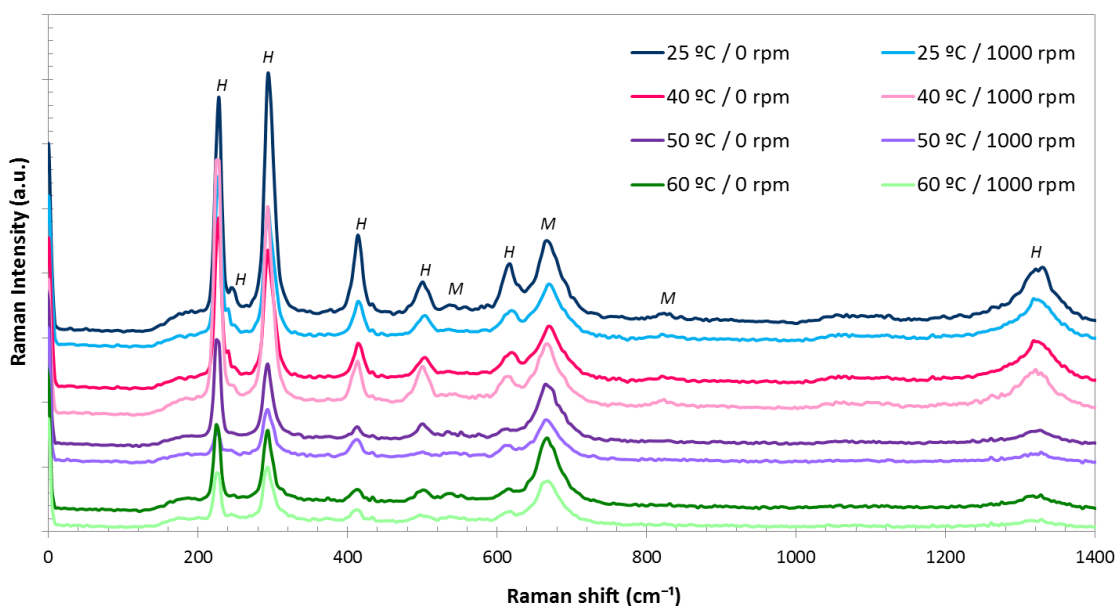
Figure 6. Raman spectra of the iron oxide nanostructures at the different electrolyte temperatures under both stagnant and hydrodynamic conditions, and annealed at 500 ⁰C in argon for 1 h. *H: Hematite (α-Fe₂O₃); M: Magnetite (Fe₃O₄).*

3.4. Electrochemical and photoelectrochemical characterization

3.4.1. Photoelectrochemical water splitting tests

Figure 7 shows the photocurrent density vs. potential plots of the synthesized nanostructures. Figure 7 a) presents the plots of the samples anodized at 0 rpm; it is noticeable that the highest values of photocurrent densities were achieved for the samples anodized at 25 and 60 ⁰C, reaching in both cases, approximately, 0.092 mA · cm^{-2} at 0.54 V (vs. Ag/AgCl). However, regarding dark current density, it is important to point out that the sample anodized at 60 ⁰C attained higher values of the dark current density line which indicates an enhancement of charge transfer processes. This indicates that the nanostructure synthesized at 25 ⁰C under stagnant conditions is

most suitable for being used as photocatalyst in water splitting measurements than the one synthesized at 60 °C. On the other hand, according to Figure 7 a), the samples anodized at 40 and 50 °C achieved lower values of photocurrent densities, i.e. ~ 0.052 and ~ 0.056 mA · cm^{-2} at 0.54 V (vs. Ag/AgCl), respectively. Comparing water splitting results (Figure 7 a)) with FE-SEM images (Figure 4) under stagnant conditions, it is remarkable that the nanostructure formed at 25 °C led to a better behavior for water splitting since its structure was more porous than the other ones, which favored facile extraction of holes from the surface [52], and some nanosheets appeared at the surface which could favor photocatalytic charge separation [53,54]. At temperatures of 40 and 50 °C the nanostructures barely presented nanosheets and, their structure was more compact, which can be an inconvenient for the extraction of holes resulting in much lower photocurrent densities. Finally, at an electrolyte temperature of 60 °C the nanostructure was composed by shorter nanosheets in clusters with some precipitated crystals and these nanosheets could lead to higher photocurrent density values [53,54].
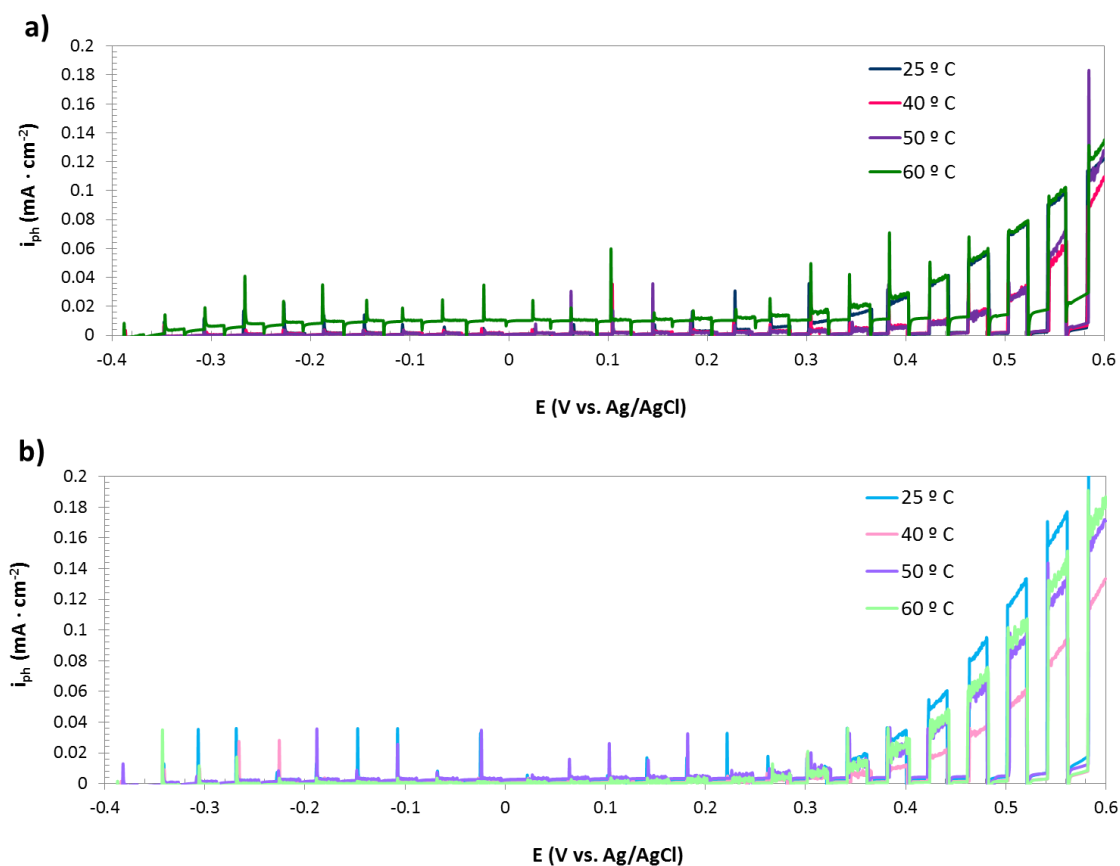
Figure 7. Photocurrent density vs. potential (water splitting) measurements obtained in 1 M KOH by applying chopped light irradiation, for the samples anodized at the different electrolyte temperatures under stagnant (a) and hydrodynamic (b) conditions. Simulated AM 1.5 illumination was used for the light conditions.

Concerning hydrodynamic conditions, Figure 7 b) shows the water splitting measurements and it is clearly seen that the highest photocurrent density values were achieved for the samples anodized at an electrolyte temperature of 25 $^{\circ}$C (~ 0.158 mA · cm^{-2} at 0.54 V (vs. Ag/AgCl)). By contrast, the samples anodized at 50 and 60 $^{\circ}$C reached lower photocurrent densities (~0.120 and ~0.130 mA · cm^{-2} at 0.54 V (vs. Ag/AgCl), respectively) but the lowest value (~0.080 mA · cm^{-2} at 0.54 V (vs. Ag/AgCl)) was achieved for the samples synthetized at 40 $^{\circ}$C. It is noticeable that in

23

this case, the sample anodized at 60 °C did not present a high value of the dark current density line, in contrast with what occurred in the case of stagnant conditions. Establishing a relation between water splitting results and morphology, Figure 5 showed that the nanostructure synthesized at 25 °C presented a morphology with some nanosheets in its surface and it was more porous than the rest of the samples, which could favor the photoresponse in the water splitting tests since hole extraction was improved [52–54]. The rest of the nanostructures possessed a more compact structure which resulted in lower photocurrent density values in the water splitting measurements (Figure 7 b)).

3.4.2. Photostability measurements

Figure 8 shows the photostability measurements of the samples anodized at the different electrolyte temperatures and under both stagnant and hydrodynamic conditions. It is seen that all the samples were stable against photocorrosion in the studied conditions, i.e. in 1 M KOH solution at 0.35 V (vs. Ag/AgCl). In the case of stagnant conditions (Figure 8 a)), the samples that achieve higher photocurrent density values were the ones synthesized at 60 and 25 °C which is in agreement with the photocurrent density vs. potential measurements (Figure 7 a)). For the nanostructures synthesized under hydrodynamic conditions (Figure 8 b)), the samples anodized at 25 and 60 °C reached higher photocurrent densities than the other ones, and this is also in agreement with the water splitting measurements (Figure 7 b)).
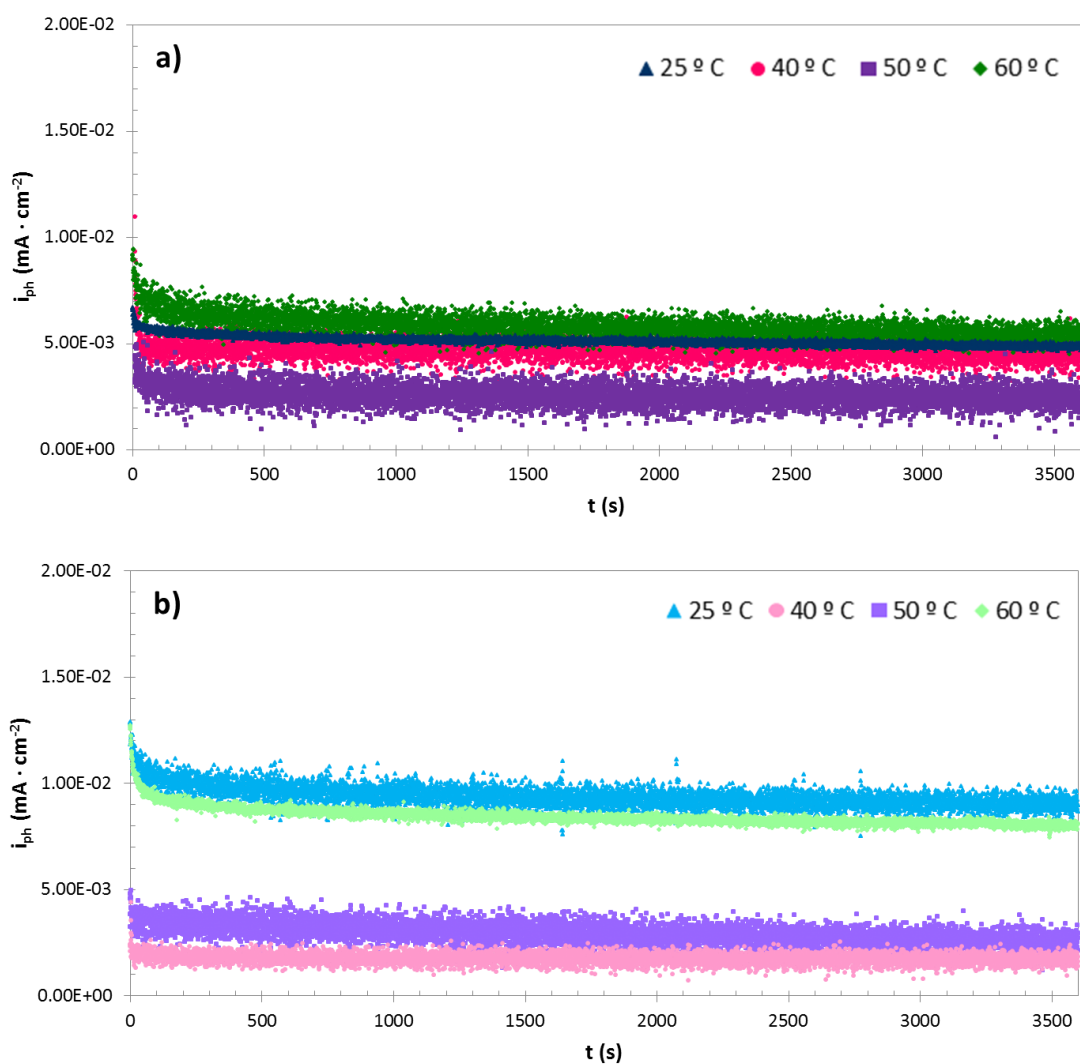
Figure 8. Photostability tests obtained in 1 M KOH at 0.35 V (vs. Ag/AgCl) under light conditions, for the samples anodized at the different electrolyte temperatures under stagnant (a) and hydrodynamic (b) conditions. Simulated AM 1.5 illumination was used for the light conditions.

3.4.3. Mott-Schottky analysis

Mott-Schottky plots (C_{SC}^{-2} vs. E) were performed in 1 M KOH under dark and light conditions for all the synthesized nanostructures and they are presented in Figure 9. Considering hematite as an n-type semiconductor being electrons the majority charge

carriers [19,25,55], the corresponding Mott-Schottky equation is presented as Eq. 3 [56,57].

$$\frac{1}{C_{SC}{}^2} = \left(\frac{2}{e \cdot \varepsilon_0 \cdot \varepsilon_r \cdot N_D}\right) \cdot \left(E - E_{FB} - \frac{k \cdot T}{e}\right) \qquad (Eq.\,3)$$

where C_{SC} is the space charge layer capacitance, E the applied potential, E_{FB} the flat band potential, k the Boltzmann constant ($1.38 \cdot 10^{23}$ J $\cdot$ K^{-1}), T the absolute temperature, e the electron charge ($1.60 \cdot 10^{-19}$ C), ε_0 the vacuum permittivity ($8.85 \cdot 10^{-14}$ F $\cdot$ cm^{-1}), ε_r the dielectric constant (considering a value of 80 for the hematite nanostructures [20,58,59]) and N_D is the donor density.
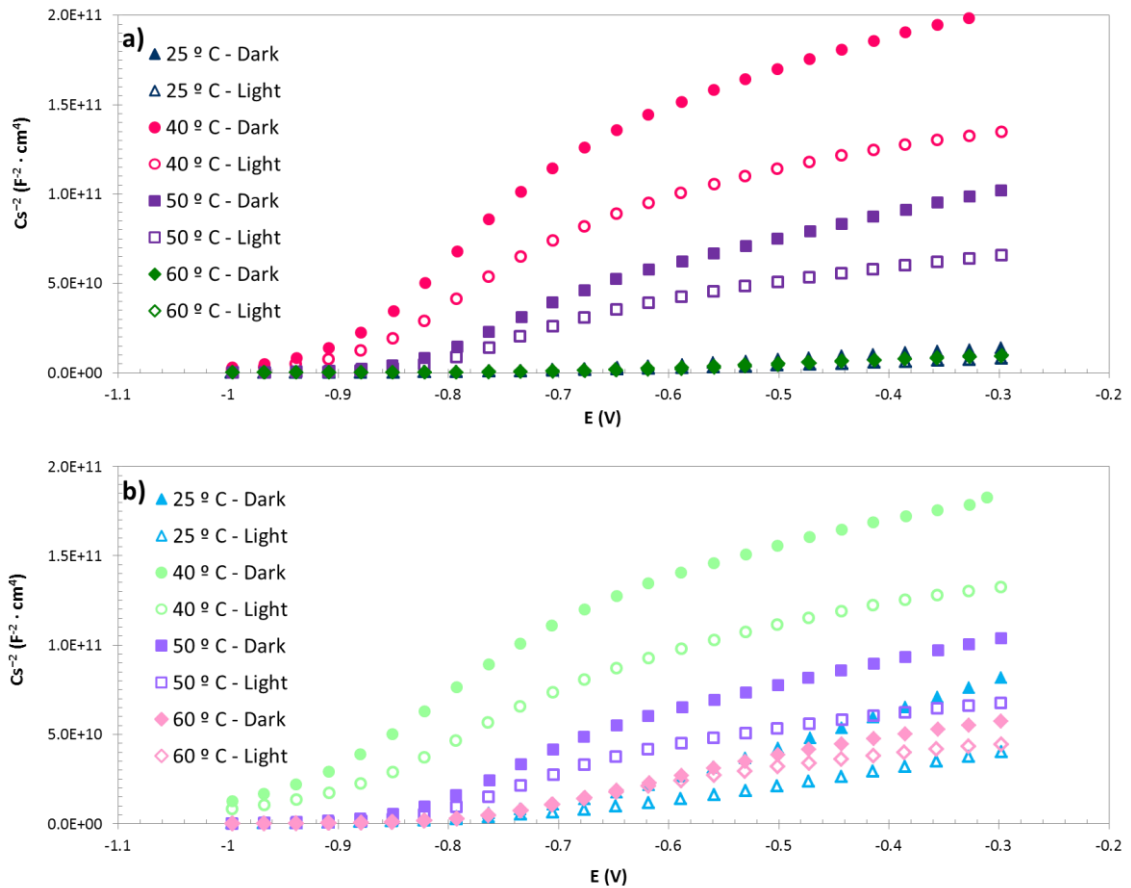

Figure 9. Mott-Schottky analysis obtained in 1 M KOH under dark and light conditions, for the samples anodized at the different electrolyte temperatures under stagnant (a) and

hydrodynamic (b) conditions. Simulated AM 1.5 illumination was used for the light conditions.

N_D values for the different samples were determined from the slopes (σ) of the quasi-linear regions in the MS plots using Eq. 4. It is noticeable that the relation is inversely proportional, then, the higher the slopes the lower the donor density values.

$$N_D = \left(\frac{2}{e \cdot \varepsilon_0 \cdot \varepsilon_r \cdot \sigma}\right) \qquad\qquad (\boldsymbol{Eq.\,4})$$

Figure 9 a) illustrates MS plots for the nanostructures anodized at the different electrolyte temperatures under stagnant conditions. The highest slopes correspond to the samples anodized at 40 °C, whereas the lowest ones correspond to the samples anodized at 25 and 60 °C. According to this, the highest N_D values are expected for the nanostructures anodized at 25 and 60 °C, and the lowest ones for the samples anodized at 40 °C. Table 1 shows the different N_D values for all the nanostructures and they are all in the order of 10^{19} cm^{-3}, which is in agreement with the literature [24,60]. Furthermore, the values of N_D under illumination are higher than the ones under dark conditions because illumination promotes charge separation increasing then donor density.

N_D values for the samples anodized at 25 and 60 °C are similar and they are the highest. However, the sample anodized at 40 °C shows the lowest values of N_D under dark and light conditions, respectively. These results are in agreement with the water splitting tests which indicated that the better photoresponse was for the samples anodized at 25 and 60 °C under stagnant conditions.

This is due to the fact that higher N_D results in an increase in the photoactivity of the nanostructures in photocatalytic application since the charge transfer kinetics are improved [24,59,61]. Then, the higher N_D values the higher electronic conductivity and, hence, the better photoactivity of the samples for water splitting applications (Figure 7). However, an increase in N_D, i.e. an increase in defects, may enhance charge recombination and this can be detrimental for the photoelectrochemical behavior in water splitting [62].

Regarding the samples anodized at the different electrolyte temperatures under hydrodynamic conditions, the highest values of N_D correspond to the samples anodized at 25 and 60 ⁰C, as Table 1 shows. This is also in agreement with the water splitting results that indicated the best photoresponse for the sample anodized at 25 ⁰C followed by the one anodized at 60 ⁰C. However, according to Table 1, the samples anodized at 40 and 50 ⁰C achieved the lowest donor density and then, the lowest photoresponse in water splitting measurements (Figure 7 b)).

Electrolyte temperature / Rotation speed	Conditions	N_D ($\cdot 10^{19}$) (cm^{-3})	E_{FB} (vs. Ag/AgCl) (V)
25 ⁰ C / 0 rpm	Dark	5.57 $\pm$ 0.53	-0.74 $\pm$ 0.05
	Light	9.78 $\pm$ 0.58	-0.74 $\pm$ 0.07
25 ⁰ C / 1000 rpm	Dark	1.02 $\pm$ 0.24	-0.76 $\pm$ 0.04
	Light	2.22 $\pm$ 0.66	-0.78 $\pm$ 0.03
40 ⁰ C / 0 rpm	Dark	0.31 $\pm$ 0.10	-0.91 $\pm$ 0.05
	Light	0.48 $\pm$ 0.12	-0.90 $\pm$ 0.05
40 ⁰ C / 1000 rpm	Dark	0.42 $\pm$ 0.10	-0.97 $\pm$ 0.07
	Light	0.59 $\pm$ 0.15	-0.95 $\pm$ 0.05
50 ⁰ C / 0 rpm	Dark	0.80 $\pm$ 0.28	-0.87 $\pm$ 0.04
	Light	1.10 $\pm$ 0.75	-0.86 $\pm$ 0.05
50 ⁰ C / 1000 rpm	Dark	0.73 $\pm$ 0.21	-0.87 $\pm$ 0.08
	Light	1.01 $\pm$ 0.42	-0.86 $\pm$ 0.05
60 ⁰ C / 0 rpm	Dark	7.09 $\pm$ 2.11	-0.69 $\pm$ 0.06
	Light	8.39 $\pm$ 2.20	-0.74 $\pm$ 0.07
60 ⁰ C / 1000 rpm	Dark	1.41 $\pm$ 0.23	-0.80 $\pm$ 0.07
	Light	1.74 $\pm$ 0.35	-0.82 $\pm$ 0.04

Table 1. Values of donor density (N_D) and flat band potential (E_{FB}) obtained in 1 M KOH under dark and light conditions, for the samples anodized at the different electrolyte temperatures under stagnant and hydrodynamic conditions. Simulated AM 1.5 illumination was used for the light conditions.

Therefore, the best photoresponse in water splitting measurements is for the sample anodized at 25 °C under hydrodynamic conditions, since its N_D is high enough to enhance the electrical conductivity but insufficient to make these defects act as carrier traps, like it might occur in the case of stagnant conditions (where the N_D values are too high).

On the other hand, as Eq. 5 shows, when the applied voltage (E) is such that there is no potential drop at the depletion space charge layer ($\Delta\phi_{SC}$), i.e. the band bending is zero, hence the semiconductor is at its flat band potential (E_{FB}) [63]. The E_{FB} of the different samples were obtained by extrapolating the quasi-linear region of the MS plots to $C^{-2} = 0$.

$$\Delta\phi_{SC} = E - E_{FB} \qquad\qquad\qquad (\textbf{\textit{Eq.}}\,\textbf{5})$$

The obtained values for the different nanostructures are approximately in the range of -0.7 to -0.9 V (Table 1), which is in agreement with the literature [64–66].

4. Conclusions

In the present study, the effect of the electrolyte temperature on the synthesis of iron oxide nanostructures by electrochemical anodization was studied in order to synthesize

suitable nanostructures for being used as photocatalyst in water splitting for hydrogen production. Different temperatures were studied: 25, 40, 50 and 60 $^\circ$C, under stagnant and hydrodynamic (in particular a rotation speed of 1000 rpm) conditions.

Results indicated that the highest photocurrent densities in the water splitting tests were achieved for the nanostructures synthesized at 25 $^\circ$C under hydrodynamic conditions. FE-SEM images showed that this nanostructure presented a porous morphology with some nanosheets appearing over the surface, which could improve its photoelectrocatalytic performance since hole extraction was enhanced. Moreover, the nanostructure was stable against photocorrosion as the photostability tests showed, and Laser Confocal Raman microscopy revealed that the crystalline structure was predominantly composed by hematite (α-Fe$_2$O$_3$) with some amount of magnetite (Fe$_3$O$_4$). Finally, the Mott-Schottky analysis indicated that the sample presented N_D values that are high enough to enhance the electrical conductivity but insufficient to make these defects act as carrier traps.

REFERENCES

[1]   Y. Li, J. Feng, H. Li, X. Wei, R. Wang, Photoelectrochemical splitting of natural seawater with a α-Fe_2O_3/WO_3 nanorod arrays, Int. J. Hydrogen Energy. 41 (2016) 4096–4105. doi:10.1016/j.ijhydene.2016.01.027.

[2]   M.M. Momeni, Y. Ghayeb, Cobalt modified tungsten–titania nanotube composite photoanodes for photoelectrochemical solar water splitting, J. Mater. Sci. Mater. Electron. 27 (2016) 3318–3327. doi:10.1007/s10854-015-4161-2.

[3]   X. Chen, S. Shen, L. Guo, S.S. Mao, Semiconductor-based Photocatalytic Hydrogen Generation., Chem. Rev. 110 (2010) 6503–6570. doi:10.1021/cr1001645.

[4]   Y. Ghayeb, M.M. Momeni, Solar water-splitting using palladium modified tungsten trioxide-titania nanotube photocatalysts, J. Mater. Sci. Mater. Electron. 27 (2016) 1805–1811. doi:10.1007/s10854-015-3957-4.

[5]   M.-C. Huang, T. Wang, W.-S. Chang, C.-C. Wu, J.-C. Lin, C.-H. Lee, et al., Effect of anodizing temperature on surface morphology evolution of sputtered hematite films: A potential post-treatment method for further photoelectrochemical performance enhancement photoelectrochemical performance enhancement, 2016. doi:10.1016/j.vacuum.2016.04.021.

[6]   M.M. Momeni, Y. Ghayeb, Fabrication, characterization and photoelectrochemical behavior of Fe-TiO_2 nanotubes composite photoanodes for solar water splitting, J. Electroanal. Chem. 751 (2015) 43–48. doi:10.1016/j.jelechem.2015.05.035.

[7]   S. Demirci, C. Sarıoğlu, Fast and low-cost fabrication of 1D hematite photoanode in pure water vapor and air atmosphere: Investigation the effect of the oxidation atmosphere on the PEC performance of the hematite photoanodes, Int. J. Hydrogen Energy. (2017). doi:10.1016/j.ijhydene.2017.01.140.

[8]   A. Fujishima, K. Honda, Electrochemical Photolysis of Water at a Semiconductor Electrode, Nat. Mater. 238 (1972) 37–38.

[9]   M.M. Momeni, Y. Ghayeb, F. Ezati, Fabrication, characterization and photoelectrochemical activity of tungsten-copper co-sensitized TiO_2 nanotube

composite photoanodes, J. Colloid Interface Sci. 514 (2018) 70–82. doi:10.1016/j.jcis.2017.12.021.

[10] J. Cai, S. Li, Z. Li, J. Wang, Y. Ren, G. Qin, Electrodeposition of Sn-doped hollow α-Fe$_2$O$_3$ nanostructures for photoelectrochemical water splitting, J. Alloys Compd. 574 (2013) 421–426. doi:10.1016/j.jallcom.2013.05.152.

[11] M.M. Momeni, Y. Ghayeb, M. Shafiei, Preparation and characterization of CrFeWTiO$_2$ photoanodes and their photoelectrochemical activities for water splitting, Dalt. Trans. 46 (2017) 12527–12536. doi:10.1039/C7DT01596H.

[12] M. Huang, T. Wang, W. Chang, C. Wu, Effect of anodizing temperature on surface morphology evolution of sputtered hematite films : A potential post-treatment method for further photoelectrochemical performance enhancement, Vaccum. 129 (2016) 111–114. doi:10.1016/j.vacuum.2016.04.021.

[13] M.M. Momeni, Y. Ghayeb, Photoelectrochemical water splitting on chromium-doped titanium dioxide nanotube photoanodes prepared by single-step anodizing, J. Alloys Compd. 637 (2015) 393–400. doi:10.1016/j.jallcom.2015.02.137.

[14] Q. Kang, J. Cao, Y. Zhang, L. Liu, H. Xu, J. Ye, Reduced TiO$_2$ nanotube arrays for photoelectrochemical water splitting, J. Mater. Chem. A. 1 (2013) 5766–5774. doi:10.1039/c3ta10689f.

[15] D. Valerini, S. Hernández, F. Di Benedetto, N. Russo, G. Saracco, A. Rizzo, Sputtered WO$_3$ films for water splitting applications, Mater. Sci. Semicond. Process. 42 (2016) 150–154. doi:10.1016/j.mssp.2015.09.013.

[16] Q. Zhang, D. Xu, X. Zhou, K. Zhang, Solar Hydrogen Generation from Water Splitting Using ZnO/CuO Hetero Nanostructures, Energy Procedia. 61 (2014) 345–348. doi:10.1016/j.egypro.2014.11.1121.

[17] N. Bhandary, A.P. Singh, P.P. Ingole, S. Basu, Enhancing the Photoelectrochemical Performance of a Hematite Dendrite/Graphitic Carbon Nitride Nanocomposite through Surface Modification with CoFeO$_x$, ChemPhotoChem. 1 (2017) 70–75. doi:10.1002/cptc.201600008.

[18] M. Mishra, D.-M. Chun, α-Fe$_2$O$_3$ as a photocatalytic material: A review, Appl. Catal. A Gen. 498 (2015) 126–141. doi:10.1016/j.apcata.2015.03.023.

[19] C. Wang, Z. Huang, Controlled synthesis of α-Fe$_2$O$_3$ nanostructures for efficient photocatalysis, Mater. Lett. 164 (2016) 194–197. doi:10.1016/j.matlet.2015.10.152.

[20] P. Dias, A. Vilanova, T. Lopes, L. Andrade, A. Mendes, Extremely Stable Bare Hematite Photoanode for Solar Water Splitting, Nano Energy. 23 (2016) 70–79. doi:10.1016/j.nanoen.2016.03.008.

[21] K. Sivula, F. Le Formal, M. Grätzel, Solar Water Splitting: Progress Using Hematite (α-Fe_2O_3) Photoelectrodes, ChemSusChem. 4 (2011) 432–449. doi:10.1002/cssc.201000416.

[22] K. Xie, J. Li, Y. Lai, W. Lu, Z. Zhang, Y. Liu, et al., Highly ordered iron oxide nanotube arrays as electrodes for electrochemical energy storage, Electrochem. Commun. 13 (2011) 657–660. doi:10.1016/j.elecom.2011.03.040.

[23] A.G. Tamirat, J. Rick, A.A. Dubale, W.-N. Su, B.-J. Hwang, Using hematite for photoelectrochemical water splitting: a review of current progress and challenges, Nanoscale Horiz. (2016). doi:10.1039/C5NH00098J.

[24] S. Shen, J. Zhou, C.-L. Dong, Y. Hu, E.N. Tseng, P. Guo, et al., Surface Engineered Doping of Hematite Nanorod Arrays for Improved Photoelectrochemical Water Splitting, Sci. Rep. 4 (2014) 6627–6636. doi:10.1038/srep06627.

[25] S.R. Pendlebury, M. Barroso, A.J. Cowan, K. Sivula, J. Tang, M. Grätzel, et al., Dynamics of photogenerated holes in nanocrystalline α-Fe_2O_3 electrodes for water oxidation probed by transient absorption spectroscopy., Chem. Commun. 47 (2011) 716–8. doi:10.1039/c0cc03627g.

[26] K. Sivula, R. Zboril, F. Le Formal, R. Robert, A. Weidenkaff, J. Tucek, et al., Photoelectrochemical Water Splitting with Mesoporous Hematite Prepared by a Solution-Based Colloidal Approach Photoelectrochemical Water Splitting with Mesoporous Hematite Prepared by a Solution-Based Colloidal Approach, J. Am. Chem. Soc. 132 (2010) 7436–7444. doi:10.1021/ja101564f.

[27] L. Wang, C.Y. Lee, P. Schmuki, Improved photoelectrochemical water splitting of hematite nanorods thermally grown on Fe-Ti alloys, Electrochem. Commun. 44 (2014) 49–53. doi:10.1016/j.elecom.2014.04.010.

[28] B. Klahr, S. Gimenez, F. Fabregat-Santiago, T. Hamann, J. Bisquert, Water oxidation at hematite photoelectrodes: The role of surface states, J. Am. Chem. Soc. 134 (2012) 4294–4302. doi:10.1021/ja210755h.

[29] R.R. Rangaraju, K.S. Raja, a. Panday, M. Misra, An investigation on room temperature synthesis of vertically oriented arrays of iron oxide nanotubes by

anodization of iron, Electrochim. Acta. 55 (2010) 785–793. doi:10.1016/j.electacta.2009.07.012.

[30]   M.M. Momeni, Y. Ghayeb, F. Mohammadi, Solar water splitting for hydrogen production with Fe_2O_3 nanotubes prepared by anodizing method: effect of anodizing time on performance of Fe_2O_3 nanotube arrays, J. Mater. Sci. Mater. Electron. 26 (2014) 685–692. doi:10.1007/s10854-014-2450-9.

[31]   L. Kopanja, I. Milosevic, M. Panjan, V. Damnjanovic, M. Tadic, Sol–gel combustion synthesis, particle shape analysis and magnetic properties of hematite (α-Fe_2O_3) nanoparticles embedded in an amorphous silica matrix, Appl. Surf. Sci. 362 (2016) 380–386. doi:10.1016/j.apsusc.2015.11.238.

[32]   S. Shivakumara, T.R. Penki, N. Munichandraiah, Preparation and electrochemical performance of porous hematite (α-Fe_2O_3) nanostructures as supercapacitor electrode material, J. Solid State Electrochem. 18 (2014) 1057–1066. doi:10.1007/s10008-013-2355-1.

[33]   E.L. Tsege, T.S. Atabaev, M.A. Hossain, D. Lee, H.-K. Kim, Y.-H. Hwang, Cu-doped flower-like hematite nanostructures for efficient water splitting applications, J. Phys. Chem. Solids. 98 (2016) 283–289. doi:10.1016/j.jpcs.2016.07.014.

[34]   A. Pu, J. Deng, Y. Hao, X. Sun, J. Zhong, Thickness effect of hematite nanostructures prepared by hydrothermal method for solar water splitting, Appl. Surf. Sci. 320 (2014) 213–217. doi:10.1016/j.apsusc.2014.09.086.

[35]   H. Wang, Y. Zhou, Y. Shen, Y. Li, Q. Zuo, Q. Duan, Fabrication, formation mechanism and the application in lithium-ion battery of porous Fe_2O_3 nanotubes via single-spinneret electrospinning, Electrochim. Acta. 158 (2015) 105–112. doi:10.1016/j.electacta.2015.01.149.

[36]   L. Burke, C.J. Mortimer, D.J. Curtis, A.R. Lewis, R. Williams, K. Hawkins, et al., In-situ synthesis of magnetic iron-oxide nanoparticle-nanofibre composites using electrospinning, Mater. Sci. Eng. C. 70 (2017) 512–519. doi:10.1016/j.msec.2016.09.014.

[37]   C.-Y. Lee, L. Wang, Y. Kado, M.S. Killian, P. Schmuki, Anodic nanotubular/porous hematite photoanode for solar water splitting: substantial effect of iron substrate purity., ChemSusChem. 7 (2014) 934–40. doi:10.1002/cssc.201300603.

[38]   Z. Zhang, M.F. Hossain, T. Takahashi, Self-assembled hematite (α-Fe_2O_3) nanotube arrays for photoelectrocatalytic degradation of azo dye under simulated

solar light irradiation, Appl. Catal. B Environ. 95 (2010) 423–429. doi:10.1016/j.apcatb.2010.01.022.

[39] B. Lucas-Granados, R. Sánchez-Tovar, R.M. Fernández-Domene, J. García-Antón, Controlled hydrodynamic conditions on the formation of iron oxide nanostructures synthesized by electrochemical anodization: Effect of the electrode rotation speed, Appl. Surf. Sci. 392 (2017) 503–513. doi:10.1016/j.apsusc.2016.09.073.

[40] B. Lucas-Granados, R. Sánchez-Tovar, R.M. Fernández-Domene, J. García-Antón, Study of the annealing conditions and photoelectrochemical characterization of a new iron oxide bi-layered nanostructure for water splitting, Sol. Energy Mater. Sol. Cells. 153 (2016) 68–77. doi:10.1016/j.solmat.2016.04.005.

[41] K. Xie, M. Guo, H. Huang, Y. Liu, Fabrication of iron oxide nanotube arrays by electrochemical anodization, Corros. Sci. 88 (2014) 66–75. doi:10.1016/j.corsci.2014.07.019.

[42] S.K. Mohapatra, S.E. John, S. Banerjee, M. Misra, Water Photooxidation by Smooth and Ultrathin α-Fe$_2$O$_3$ Nanotube Arrays, Chem. Mater. 21 (2009) 3048–3055. doi:10.1021/cm8030208.

[43] S.A. Pervez, D. Kim, U. Farooq, A. Yaqub, J.H. Choi, Y.J. Lee, et al., Crystalline iron oxide nanotube arrays with high aspect ratio as binder free anode for Li-ion batteries, Phys. Status Solidi Appl. Mater. Sci. 211 (2014) 1889–1894. doi:10.1002/pssa.201330537.

[44] T. Aerts, I. De Graeve, H. Terryn, Control of the electrode temperature for electrochemical studies: A new approach illustrated on porous anodizing of aluminium, Electrochem. Commun. 11 (2009) 2292–2295. doi:10.1016/j.elecom.2009.10.013.

[45] T. Aerts, J.B. Jorcin, I. De Graeve, H. Terryn, Comparison between the influence of applied electrode and electrolyte temperatures on porous anodizing of aluminium, Electrochim. Acta. 55 (2010) 3957–3965. doi:10.1016/j.electacta.2010.02.044.

[46] J.M. Macak, H. Hildebrand, U. Marten-Jahns, P. Schmuki, Mechanistic aspects and growth of large diameter self-organized TiO$_2$ nanotubes, J. Electroanal. Chem. 621 (2008) 254–266. doi:10.1016/j.jelechem.2008.01.005.

[47] K. Yasuda, P. Schmuki, Control of morphology and composition of self-organized zirconium titanate nanotubes formed in (NH$_4$)$_2$SO$_4$/NH$_4$F electrolytes,

Electrochim. Acta. 52 (2007) 4053–4061. doi:10.1016/j.electacta.2006.11.023.

[48]   A.M. Jubb, H.C. Allen, Vibrational spectroscopic characterization of hematite, maghemite, and magnetite thin films produced by vapor deposition, ACS Appl. Mater. Interfaces. 2 (2010) 2804–2812. doi:10.1021/am1004943.

[49]   M. Lübbe, A.M. Gigler, R.W. Stark, W. Moritz, Identification of iron oxide phases in thin films grown on Al_2O_3(0001) by Raman spectroscopy and X-ray diffraction, Surf. Sci. 604 (2010) 679–685. doi:10.1016/j.susc.2010.01.015.

[50]   S. Nie, E. Starodub, M. Monti, D. a. Siegel, L. Vergara, F. El Gabaly, et al., Insight into magnetite's redox catalysis from observing surface morphology during oxidation, J. Am. Chem. Soc. 135 (2013) 10091–10098. doi:10.1021/ja402599t.

[51]   D.L. a de Faria, F.N. Lopes, Heated goethite and natural hematite: Can Raman spectroscopy be used to differentiate them?, Vib. Spectrosc. 45 (2007) 117–121. doi:10.1016/j.vibspec.2007.07.003.

[52]   H.-J. Ahn, M.-J. Kwak, J.-S. Lee, K.-Y. Yoon, J.-H. Jang, Nanoporous hematite structures to overcome short diffusion lengths in water splitting, J. Mater. Chem. A. 2 (2014) 19999–20003. doi:10.1039/C4TA04890C.

[53]   P. Peerakiatkhajohn, J.H. Yun, H. Chen, M. Lyu, T. Butburee, L. Wang, Stable Hematite Nanosheet Photoanodes for Enhanced Photoelectrochemical Water Splitting, Adv. Mater. 28 (2016) 6405–6410. doi:10.1002/adma.201601525.

[54]   J. Liu, Y.Y. Cai, Z.F. Tian, G.S. Ruan, Y.X. Ye, C.H. Liang, et al., Highly oriented Ge-doped hematite nanosheet arrays for photoelectrochemical water oxidation, Nano Energy. 9 (2014) 282–290. doi:10.1016/j.nanoen.2014.08.005.

[55]   G. Rahman, O.-S. Joo, Photoelectrochemical water splitting at nanostructured α-Fe_2O_3 electrodes, Int. J. Hydrogen Energy. 37 (2012) 13989–13997. doi:10.1016/j.ijhydene.2012.07.037.

[56]   F. Le Formal, N. Tétreault, M. Cornuz, T. Moehl, M. Grätzel, K. Sivula, Passivating surface states on water splitting hematite photoanodes with alumina overlayers, Chem. Sci. 2 (2011) 737. doi:10.1039/c0sc00578a.

[57]   S.S. Shinde, R.A. Bansode, C.H. Bhosale, K.Y. Rajpure, Physical properties of hematite α-Fe_2O_3 thin films: application to photoelectrochemical solar cells, J. Semicond. 32 (2011) 013001–013009. doi:10.1088/1674-4926/32/1/013001.

[58]   Y.-J. Chen, L.-Y. Chen, The study of carrier transfer mechanism for nanostructural hematite photoanode for solar water splitting, Appl. Energy. 164 (2016) 924–933. doi:10.1016/j.apenergy.2015.08.105.

[59]   P.S. Shinde, A. Annamalai, J.H. Kim, S.H. Choi, J.S. Lee, J.S. Jang, Exploiting the dynamic Sn diffusion from deformation of FTO to boost the photocurrent performance of hematite photoanodes, Sol. Energy Mater. Sol. Cells. 141 (2015) 71–79. doi:10.1016/j.solmat.2015.05.020.

[60]   X. Lu, Y. Zeng, M. Yu, T. Zhai, C. Liang, S. Xie, et al., Oxygen-deficient hematite nanorods as high-performance and novel negative electrodes for flexible asymmetric supercapacitors, Adv. Mater. 26 (2014) 3148–3155. doi:10.1002/adma.201305851.

[61]   J.Y. Kim, G. Magesh, D.H. Youn, J.-W. Jang, J. Kubota, K. Domen, et al., Single-crystalline, wormlike hematite photoanodes for efficient solar water splitting, Sci. Rep. 3 (2013) 2681–2689. doi:10.1038/srep02681.

[62]   D. Wang, X. Zhang, P. Sun, S. Lu, L. Wang, C. Wang, et al., Photoelectrochemical water splitting with rutile TiO_2 nanowires array: Synergistic effect of hydrogen treatment and surface modification with anatase nanoparticles, Electrochim. Acta. 130 (2014) 290–295. doi:10.1016/j.electacta.2014.03.024.

[63]   K. Gelderman, L. Lee, S.W. Donne, Flat-Band Potential of a Semiconductor : Using the Mott – Schottky Equation, J. Chem. Educ. 84 (2007) 685–688.

[64]   J.A. Glasscock, P.R.F. Barnes, I.C. Plumb, N. Savvides, Enhancement of photoelectrochemical hydrogen production from hematite thin films by the introduction of Ti and Si, J. Phys. Chem. C. 111 (2007) 16477–16488. doi:10.1021/jp074556l.

[65]   A.A. Tahir, K.G. Upul Wijayantha, S. Saremi-Yarahmadi, M. Maznar, V. McKee, Nanostructured α-Fe_2O_3 thin films for photoelectrochemical hydrogen generation, Chem. Mater. 21 (2009) 3763–3772. doi:10.1021/cm803510v.

[66]   R.R. Rangaraju, A. Panday, K.S. Raja, M. Misra, Nanostructured anodic iron oxide film as photoanode for water oxidation, J. Phys. D. Appl. Phys. 42 (2009) 135303–135313. doi:10.1088/0022-3727/42/13/135303.